Acta Oceanol. Sin., 2023, Vol. 42, No. 5, P. 1–13
https://doi.org/10.1007/s13131-022-2085-2
http://www.aosocean.com
E-mail: ocean2@hyxb.org.cn

Subthermocline eddies carrying the Indonesian Throughflow water observed in the southeastern tropical Indian Ocean

Guangbing Yang[1, 2, 3], Quanan Zheng[4], Xuejun Xiong[1, 2, 3*]

[1] First Institute of Oceanography, and Key Laboratory of Marine Science and Numerical Modeling, Ministry of Natural Resources, Qingdao 266061, China

[2] Laboratory for Regional Oceanography and Numerical Modeling, Pilot National Laboratory for Marine Science and Technology (Qingdao), Qingdao 266237, China

[3] Shandong Key Laboratory of Marine Science and Numerical Modeling, Qingdao 266061, China

[4] Department of Atmospheric and Oceanic Science, University of Maryland, College Park 20742, USA

Received 12 April 2022; accepted 3 August 2022

Abstract

We observed a subthermocline eddy (STE) with a cold and fresh core during an observation cruise along a transect of 10°S in the southeastern tropical Indian Ocean (SETIO) in December 2017. The vertical scale, speed radius, and maximum swirl velocity of the STE were about 200 m, 55 km, and 0.5 m/s, respectively. The mean Rossby number and Burger number of the STE were then estimated to be about –0.7 and 2.4, indicating the STE was a submesoscale coherent vortex. The STE core water had characteristics of the Indonesian Throughflow (ITF) water and was distinct from that of surrounding areas. By examining Argo float data, another STE was well captured by five successive profiles of the same Argo float. Both STEs showed significant temperature and salinity anomalies at the σ_0=26.0–26.5 kg/m^3 surfaces. With the assumption that the low-salinity ITF water parcels could be carried only by surface eddies and the STEs, the Argo profiles, which detected low-salinity ITF water and were located outside a surface eddy, were believed to be inside an STE and were used to analyze the distribution, origin, and generation mechanism of the STE. The results suggested that the STEs carrying ITF water may be generated under topography-current interaction at the eastern coastal waters or under front-induced subduction in the area away from coastal waters. Those STEs may be widely distributed in the SETIO and may play a role in ITF water parcel transport.

Key words: subthermocline eddy, southeastern tropical Indian Ocean, Indonesian Throughflow, submesoscale coherent vortex

Citation: Yang Guangbing, Zheng Quanan, Xiong Xuejun. 2023. Subthermocline eddies carrying the Indonesian Throughflow water observed in the southeastern tropical Indian Ocean. Acta Oceanologica Sinica, 42(5): 1–13, doi: 10.1007/s13131-022-2085-2

1 Introduction

The Indonesian Throughflow (ITF) is a low-latitude connection between the Pacific and the Indian Ocean (Sprintall et al., 2009; Wang et al., 2019). It transports warm and low-salinity water from the Pacific into the Indian Ocean and affects the heat and mass budgets and air–sea heat fluxes of the two oceans (Gordon et al., 2003; Zhou et al., 2008; Van Sebille et al., 2014). The ITF exits from the Pacific into the southeastern tropical Indian Ocean (SETIO) primarily through the Ombai Strait, the Lombok Strait, and the Timor Passage (Godfrey, 1996). The ITF waters at different depths follow different spreading pathways in the Indian Ocean (Song et al., 2004; Valsala and Ikeda, 2007). Previous studies have suggested that the upper-layer of the ITF waters (above ~200 m) are advected westward by the South Equator Current, whereas the deeper ITF waters mainly flow southward (Song et al., 2004). A recent study suggested that the ITF water also may flow northwestward within the South Java Current (Makarim et al., 2019). Because diffusion and mixing tend to destroy the salinity and temperature properties of water masses, previous studies on ITF water spreading mainly have been based on tracer experiments or ITF water fraction analysis (Song et al., 2004; Valsala and Ikeda, 2007; Makarim et al., 2019).

Oceanic eddies are abundant and ubiquitous in the ocean. They play an important role in water mass transport (Zhang et al., 2014), oceanic mixing (Zhang et al., 2019), and biogeochemical processes (Yang et al., 2019a) and thus draw a lot of attention. Based on their vertical structure, oceanic eddies can be categorized as surface eddies or subsurface eddies (Song et al.,

Foundation item: The Shandong Provincial Natural Science Foundation under contract No. ZR2022MD080; the Basic Scientific Fund for National Public Research Institutes of China under contract No. 2017Q01; the National Natural Science Foundation of China (NSFC) under contract Nos 41706038, 41576027, 41376038, and 40406009; the NSFC-Shandong Joint Fund for Marine Science Research Centers under contract Nos U1406405 and U1606405; the International Cooperation Project of Indo-Pacific Ocean Environment Variation and Air-Sea Interaction under contract No. GASI-03-IPOVAI-05; the National Programme on Global Change and Air-Sea Interaction under contract Nos GASI-03-01-01-02 and GASI-IPOVAI-01-05; the Public Science and Technology Research Funds Projects of Ocean under contract No. 2009050240; the National Key Scientific Instrument and Equipment Development Projects under contract No. 2012YQ12003908; the National Science and Technology Major Project under contract No. 2016ZX05057015.
*Corresponding author, E-mail: xiongxj@fio.org.cn

2019), which have their maximum velocities at surface and at subsurface with depths ranging from tens to thousands of meters, respectively (Fig. 1). Both surface and subsurface eddies have anticyclonic and cyclonic types. The surface anticyclonic eddy (AE) has positive sea-level anomaly (SLA) and downward domed isopycnals, whereas the surface cyclonic eddy (CE) has negative SLA and upward domed isopycnals. The number of surface AEs usually is close to the number of local surface CEs (Chelton et al., 2011). The isopycnals of subsurface AEs have a double-convex lens structure, whereas the isopycnals of subsurface CEs have double-concave lens structure. Observations suggest the subsurface AEs are much more abundant than the subsurface CEs (Yang et al., 2019b).

Subthermocline eddies (STEs) are a type of subsurface eddy (Zhang et al., 2015, 2022; Hu et al., 2022). Their cores are below the thermocline and they typically have anticyclonic lenses of relatively homogenous water. STEs usually are long-lived and can move far from their origins (Bashmachnikov et al., 2015). They retain much of the characteristics of their formation area, therefore, they have an important effect on mass and heat transport in the ocean subsurface layer (Zhang et al., 2017). In addition, STEs also have an important effect on ocean mixing. Recent studies have shown that anticyclonic STE can elevate diapycnal mixing and can reflect downward propagating near inertial waves (Zhang et al., 2019). Because STEs have small or no surface signatures, they are rarely observed and are less understood. *In situ* observations, such as cruise and mooring observations, are the best way to collect this kind of data. Until now, STEs have been observed sporadically in the Northeast Atlantic (Mediterranean water eddies, Meddies; Bashmachnikov et al., 2015), the California coast (California Undercurrent eddies, Cuddies; Pelland et al., 2013), the Peru-Chile coast (Contreras et al., 2019), the northwest Indian Ocean (Red Sea water eddies, Reddies; Shapiro and Meschanov, 1991), and the Northwest Pacific (Kuroshio Extension intermediate-layer eddies, Kiddies; Li et al., 2017b). In the SETIO, a kind of cyclonic STE has been reported using *in situ* observations (Yang et al., 2019b).

In this study, we observed a kind of anticyclonic STE carrying ITF water in the SETIO. The spatial distribution of the STE was examined using Argo float data. We also discussed the origin, generation mechanism, and contribution to ITF water transport. In Section 2, we introduce the cruise observation and data. In Section 3, we illustrate the two STEs observed during cruise and captured by an Argo float. In Section 4, we discuss the distribution, origin, and generation mechanism of the STEs. Our conclusions are presented in Section 5.

2 Data and methods

2.1 *Cruise observation*

We conducted the cruise observation along the transect of 10°S in the SETIO from December 3 to 4, 2017. We employed a 38-kHz ocean surveyor vessel-mounted acoustic Doppler current profiler (VADCP, Teledyne RD Instruments) to measure the current velocity with the first bin at depth of 33 m and the bin size of 16 m. The VADCP data were first averaged into 5-min intervals and then interpolated to a horizontal spacing of 2 000 m. The VADCP observation transect was zonal from 95°E to 100°E, as marked by the red line in Fig. 2. As shown in Fig. 2, the surface current at depth of 33 m measured by VADCP was in general agreement with the geostrophic currents derived from SLA data. We used a lowered SeaBird SBE 911 Conductivity-Temperature-Depth (CTD) profiler to measure the conductivity and temperature profiles at five stations, which were coded s-1 to s-5 from west to east. The temperature and conductivity sensors were carefully calibrated in the laboratory before the cruise. The uncertainties were better than 0.001℃ and 0.000 1 S/m. After quality control, the temperature and salinity data were averaged into 1-m bins.

2.2 *Additional data*

The SLA and corresponding surface geostrophic currents with a (1/4)°×(1/4)° resolution were downloaded from the Copernicus

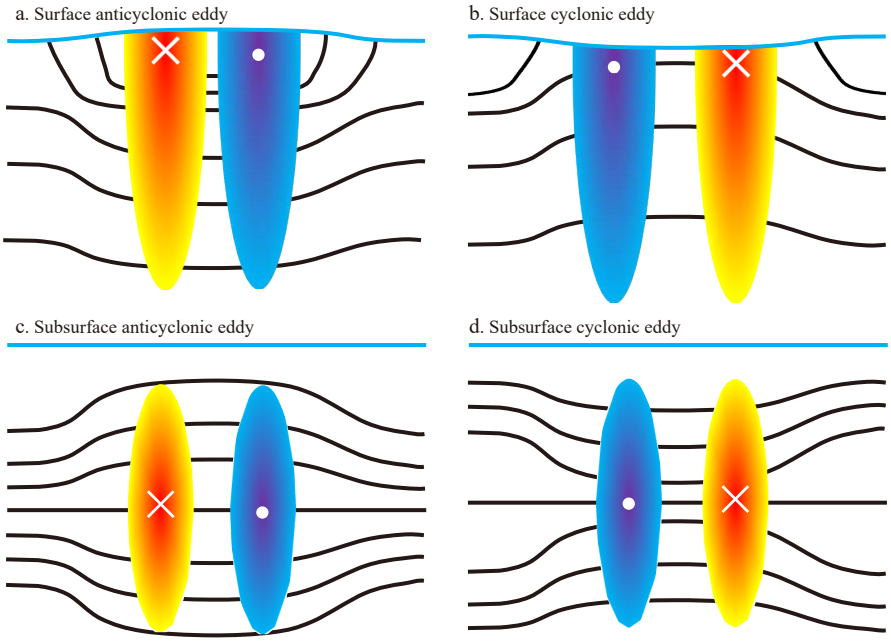

Fig. 1. Schematic showing the zonal transection of surface and subsurface eddies (in the northern hemisphere). The blue lines indicate the sea-level anomaly. The black lines indicate the isopycnals. The color shading indicates the meridional current velocity generated by eddies. The white dots and crosses indicate the southward and northward current directions, respectively.

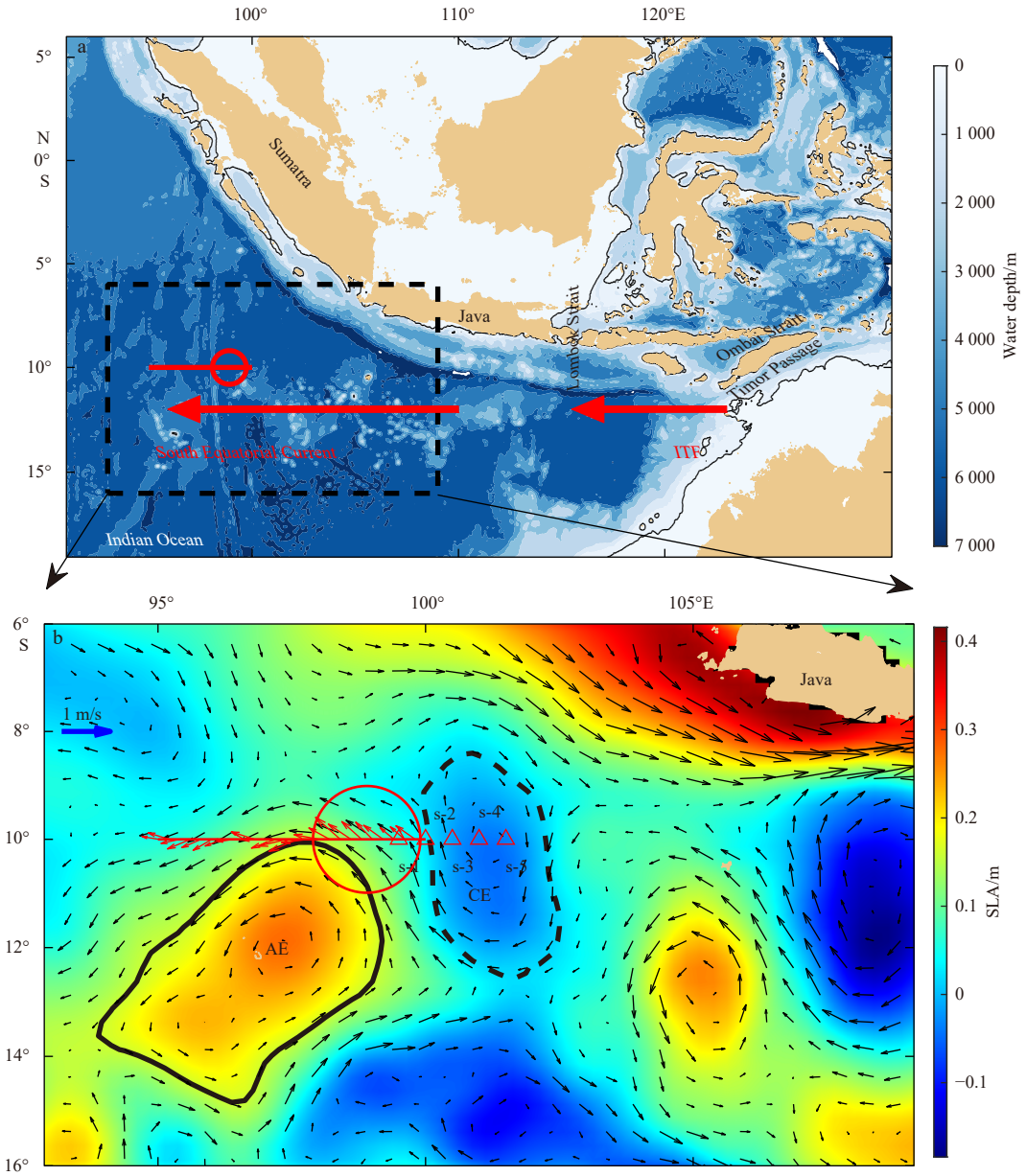

Fig. 2. The observation area and the sea-level anomaly (SLA) during observation. a. Map of the observation area in the southeastern tropical Indian Ocean. Black contours indicate the 200-m isobath. b. Color codes showing the SLA on December 3, 2017. Black solid and dashed contours show the outermost enclosed SLA isolines of the surface anticyclonic eddy (AE) and cyclonic eddy (CE), respectively. Black arrows represent geostrophic current vectors. Red arrows show the current vectors measured by vessel-mounted acoustic Doppler current profiler (VADCP) at the 33-m depth (first layer). The red triangles represent the Conductivity-Temperature-Depth stations. The red circle in a and b represents the location of the cruise-observed subthermocline eddy. The red straight lines in a and b represent the transect for VADCP observation. ITF: Indonesian Throughflow.

Marine Environment Monitoring Service (http://marine.copernicus.eu/). The surface geostrophic current data were used to calculate surface eddy kinetic energy (EKE).

We downloaded the Argo profiles data and the annual grided Argo-climatology-data (2004–2017) with 1°×1° resolution (BOA_Argo, Li et al., 2017a) from the China Argo Real-time Data Center (ftp://data.argo.org.cn/pub/ARGO/). The BOA_Argo-data had 58 vertical levels from the surface to a depth of 1 975 m. The vertical intervals were 5 m, 10 m, 20 m, and 50 m at 0–10 m, 20–170 m, 180–460 m, and 500–1 300 m, respectively. The Argo profile data were used to detect low-salinity ITF water parcels. The grided Argo-climatology-data were used to conduct water mass analysis.

We downloaded the Mesoscale Eddy Trajectory Atlas Product (META3.1exp DT, DOI: 10.24400/527896/a01-2021.001) from https://www.aviso.altimetry.fr. The META data were used to present the locations and radii of the surface eddies.

3 Results

3.1 *STE carrying ITF water observed during the cruise*

Figures 3a and b show the currents observed along the VADCP transect. As shown in Fig. 2, the VADCP transect crossed the northern periphery of large AE, the meridional velocity in the

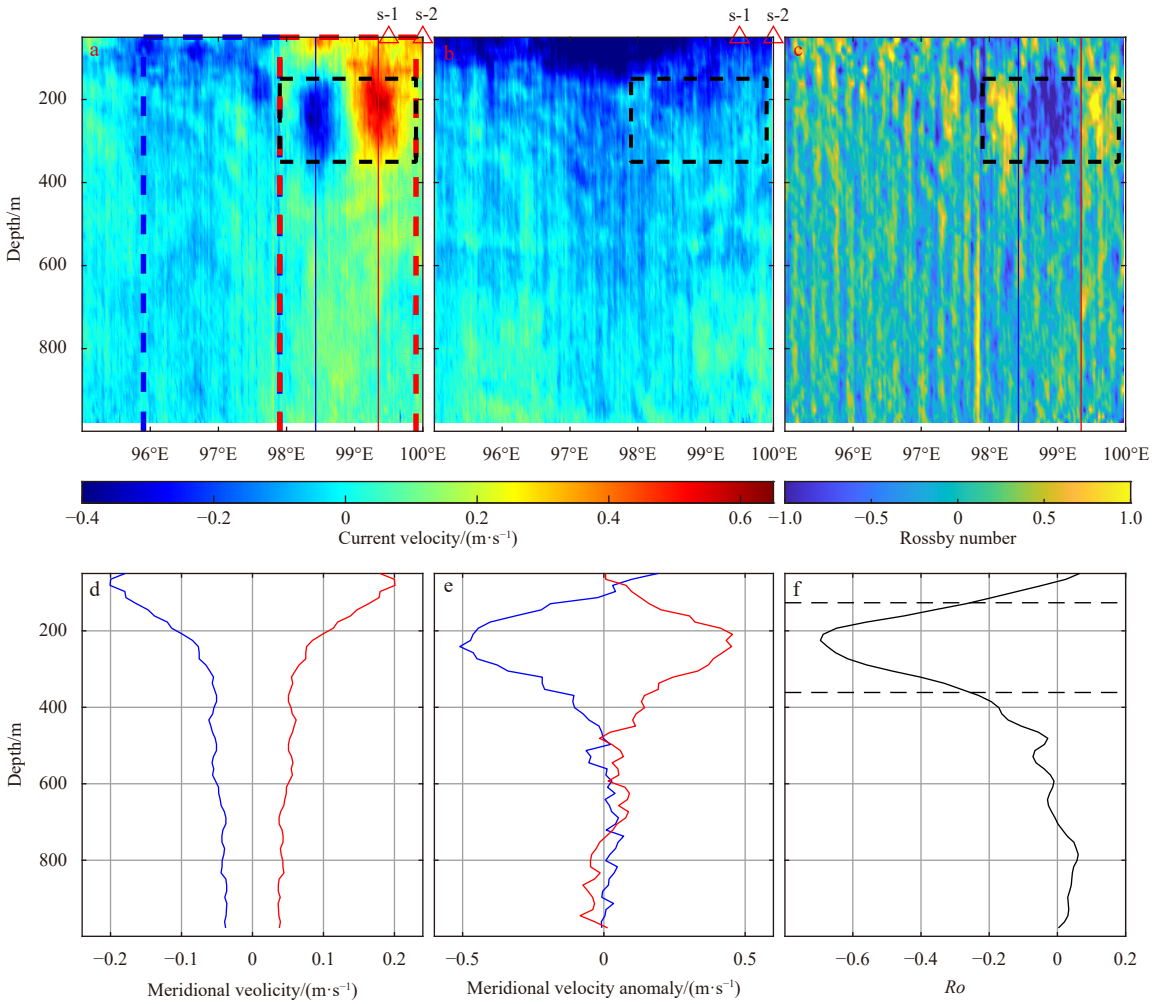

Fig. 3. Vertical distribution of the current velocity and the Rossby number. a. Meridional velocity measured along the vessel-mounted acoustic Doppler current profiler (VADCP) transect. Blue and red dashed boxes represent the western and eastern sides of the surface anticyclonic eddy (AE), respectively. The black dashed box endorses the cruise-observed subthermocline eddy (STE). Blue and red vertical lines show positions of maximum southward and northward velocities, respectively. Locations of Conductivity-Temperature-Depth stations are denoted at the top of the panel. b and c are the same as a, but for the zonal velocity and the Rossby number *Ro*, respectively. d. The blue and red lines represent the horizontally averaged meridional velocity profiles of the western and eastern sides of the AE, respectively. e. The blue and red lines represent the STE-induced meridional velocity anomaly (the VADCP-measured velocity minus the horizontally averaged meridional velocity profiles of the eastern side of the AE) at the position marked by the blue and red lines in a, respectively. f. Vertical distribution of the *Ro* averaged between the blue and red lines indicated in a and c. The two horizontal dashed lines indicate the *e*-folding vertical length scale of the STE.

western half of the transect (blue dashed box in Fig. 3a) was mainly southward, whereas the meridional current in the eastern half of the transect (red dashed box in Fig. 3a) was mainly northward. The zonal velocities along the VADCP transect were mainly westward (Fig. 3b). The horizontally averaged meridional velocities on the western and eastern sides of the AE were symmetrical (Fig. 3d). The meridional velocities had the maximum magnitudes of ~0.2 m/s near the surface and generally were on the order of 0.05 m/s in the upper 1 000 m. This velocity structure was consistent with that of the composite eddies derived from the Argo data in the SETIO (Yang et al., 2015).

As shown by the black box in Fig. 3a, a feature with strong meridional velocities was located at 150–350 m. The meridional velocity directions were southward in the western part and northward in the eastern part. In contrast to the meridional velocities, no significant zonal velocity variation could be detected, as shown by the black dashed box in Fig. 3b. The locations of the maximum southward and northward meridional velocities are marked in Fig. 3a with blue and red vertical lines at 98.4°E and 99.4°E, respectively. We calculated the meridional velocity anomaly profiles at the two locations by removing the horizontally averaged meridional velocities in the eastern part of the AE, as shown in Fig. 3e. The meridional velocity anomaly profiles with the maximum magnitudes of ~0.5 m/s at depth of 240 m were symmetric. In the southern hemisphere, these VADCP-observed meridional and zonal velocity variations indicated a subsurface anticyclonic circulation (SAC) feature. The SAC-induced zonal velocity was insignificant (Fig. 3b), implying that the VADCP transect crossed near the center of the SAC feature and the maximum swirl velocity of the SAC was ~0.5 m/s.

The temperature and salinity profiles measured at CTD stations are shown in Figs 4a and b. The isothermals below the SAC were slightly depressed, whereas the isothermals above the SAC were slightly elevated. The salinity observations showed that the

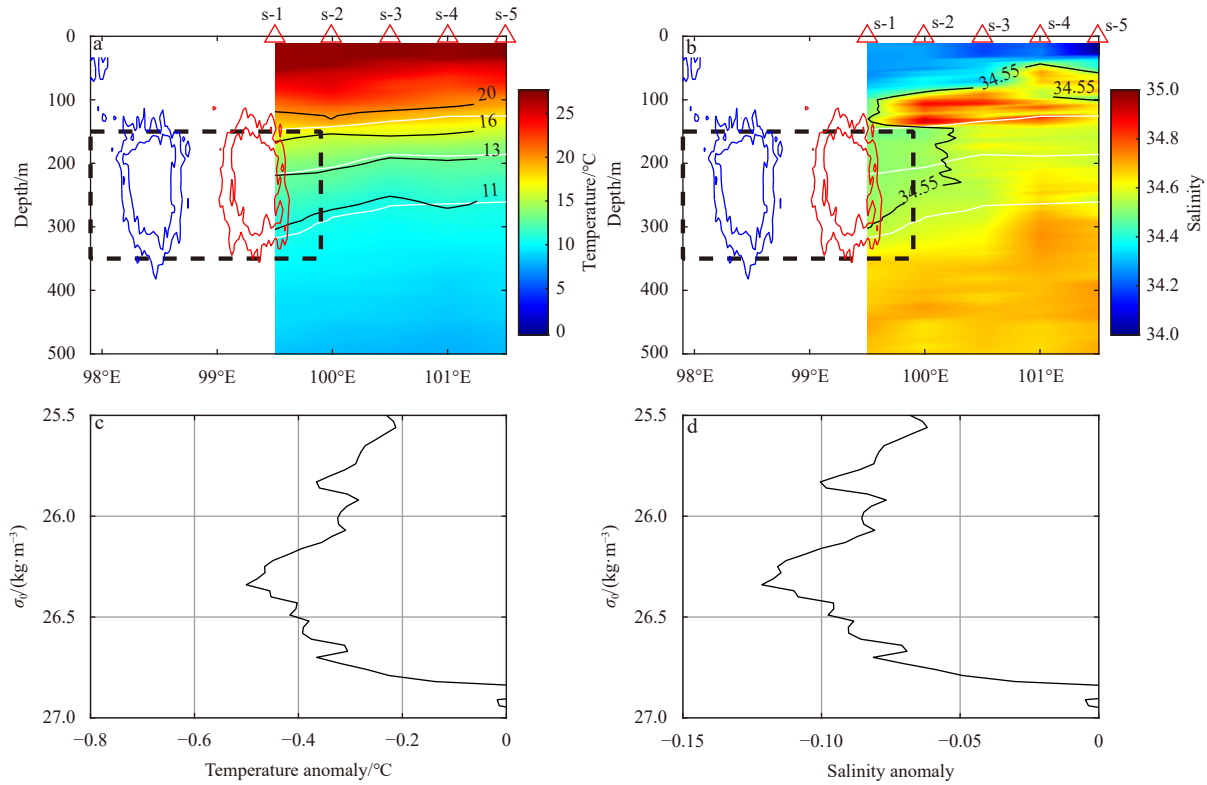

Fig. 4. Vertical distribution of the temperature, salinity, and their anomalies. a. Depth-longitude plot of water temperature observed along the Conductivity-Temperature-Depth transect. The black contours represent the isothermals of 11℃, 13℃, 16℃, and 20℃. The white contours from up and down denote isopycnals of 25 σ_0, 26 σ_0, and 26.50 σ_0, respectively. The thick (thin) blue and red contours indicate the subthermocline eddy (STE)-induced meridional velocity anomaly isolines of –0.3 m/s (–0.2 m/s) and 0.3 m/s (0.2 m/s), respectively. The black dashed box shows the cruise-observed STE area. Observation station locations are denoted at the panel top. The image in b is the same as the image a, but for the salinity. Black contour represents the isohaline of 34.55. c. The temperature anomaly generated by the cruise-observed STE, that is, the temperature at s-1 minus that at s-4. The image in d is the same as image c, but for the salinity anomaly.

SAC feature had a low-salinity core (<34.55, at ~26 σ_0 (26 σ_0 express σ_0=26 kg/m^3)). Even though the CTD transect covered only the eastern part of the SAC feature, the existence of a lens-like structure with nearly homogenous salinity was obvious within the SAC feature. As the SAC feature was distributed below the thermocline (defined by 18℃ isothermal), the temperature, salinity, and velocity distribution characteristics indicated that the SAC was an STE with a lens-like structure. The temperature and salinity anomalies against σ_0 are shown in Figs 4c and d, and significant temperature and salinity anomalies are located at the 26.0–26.5 σ_0 surfaces. The negative temperature and salinity anomalies suggested the STE carried cold and fresh water.

As the VADCP transect crossed near the STE center, we estimated the horizontal scale from its meridional velocity variations. The speed radius of the STE, defined as the range from the eddy center to the maximum axial velocity (Chelton et al., 2011), was about 55 km, which was smaller than the first baroclinic deformation radius in the observation area (about 120 km, Chelton et al., 1998). The Rossby number $Ro = \zeta/f$, where ζ is the relative vorticity, and f is the local Coriolis frequency, was calculated to reveal the dynamic feature of the STE. As the current field was measured along a zonal transection, and according to the Rankine vortex model (Zhang et al., 2022), the relative vorticity ($\zeta = \frac{\partial v}{\partial x} - \frac{\partial u}{\partial y}$, Huang et al., 2020) of the STE was approximated by $\zeta = 2\frac{\partial v}{\partial x}$, where v is the STE-induced meridional velocity anomaly. As shown in the Figs 3c and f, the largest *Ro* value is about –1.2 at a depth of 225 m and the corresponding mean *Ro* between the two STE-induced meridional velocity anomaly maximums is –0.7. The *e*-folding vertical length scale (H_e) of the STE, estimated using the vertical distribution of *Ro* (Fig. 3f), was 235 m. The Burger number of the STE was then estimated to be 2.4 with $Bu = \frac{N^2 H_e^2}{f^2 R^2}$, where N is the mean buoyancy frequency between the *e*-folding vertical scope, and R is the STE radius (Zhang et al., 2022). These results suggested the observed STE was a submesoscale eddy, that is, a submesoscale coherent vortex (Zheng et al., 2008, 2020; Mcwilliams, 2016; Yang et al., 2019c).

The most prominent feature of the STE observed on the cruise was the low-salinity core. With the assumption that STEs migrated along the isopycnal surfaces and the properties of water (such as salinity, potential temperature, and dissolved oxygen) carried by STEs were conserved during the migration (Zhang et al., 2015, 2017; Yang et al., 2019b), it was possible to trace the STE core water back to its source by finding an area that had the same water properties with the STE core. The STE core was at ~26 σ_0 (~230 m at station s-1), and the distribution of annual mean salinity of the BOA_ARGO in the Indian Ocean on the 26 σ_0 surface is shown in Fig. 5a. A westward spreading phenomenon of the low-salinity ITF water is marked by a ''tongue'' configuration centered at ~10°S in the isohalines. The 34.55 isohaline, which is located near the eastern coastal waters, was discontinuous because the annual mean Argo data were unavail-

able near the coast. Figure 5b shows the annual mean salinity distribution of the BOA_ARGO along the transect of 10°S. The salinity in the SETIO increased with depth and the low-salinity water (<34.55) on the density surfaces of the STE was located off the east of 115°E. We further illustrated the potential temperature and salinity (*T*-*S*) distribution of the CTD observations and the annual mean Argo data in Fig. 5c. The annual mean salinity of the water in the green dashed box in Fig. 5a was higher than 34.55 between 25.1 σ_0 and 26.8 σ_0 surfaces, whereas the water in the red dashed box in Fig. 5a was fresher. The STE core (station s-1, red dotted line) was characterized by the low salinity between 25.5 σ_0 and 26.5 σ_0 surfaces, which had distinct characteristics from the surrounding areas (blue dotted line and green shading), but was similar to that of the eastern coastal waters shown in the red dashed box in Fig. 5a (red shading). These results suggested that the only source of the low-salinity water in the SETIO was the ITF and the STE should carry ITF water.

3.2 *STE carrying ITF water observed by Argo floats*

Zhang et al. (2017) detected global STEs using Argo profiles by finding low potential vorticity (PV) inside a lens structure outlined by isopycnals. As shown in Fig. 4, however, the STE was located just below the thermocline and a surface AE, which tended to flatten the upper isopycnal of the lens structure and made it difficult to identify the lens structure. In addition, the STEs propagated westward in the SETIO because of the self-translation (Bashmachnikov et al., 2015) and the background current (Zhang et al., 2015). The self-translation velocity, estimated with $V_m = \beta R^2$ (Bashmachnikov et al., 2015), where β is the meridional gradient of the Coriolis parameter and R is the radius of the STE, was about 0.08 m/s. The background current was strong due to the westward South Equator Current (O(0.1 m/s), Feng and Wijffels, 2002; Yang et al., 2015) and surface eddies (O(0.1 m/s), Yang et al., 2015) at a depth of 200 m, where the cruised-observed STE was located. The background current was weak, however, at a depth of 1 000 m, where the Argo float parked for about 9 days during a typical duty cycle. The advection velocity difference (~0.1 m/s) between depths of 200 m and 1 000 m caused a horizontal distance difference of about 80 km in 9 days, making the STE was difficult to be successively sampled by a same Argo float. All of this led to the difficulty in identifying the

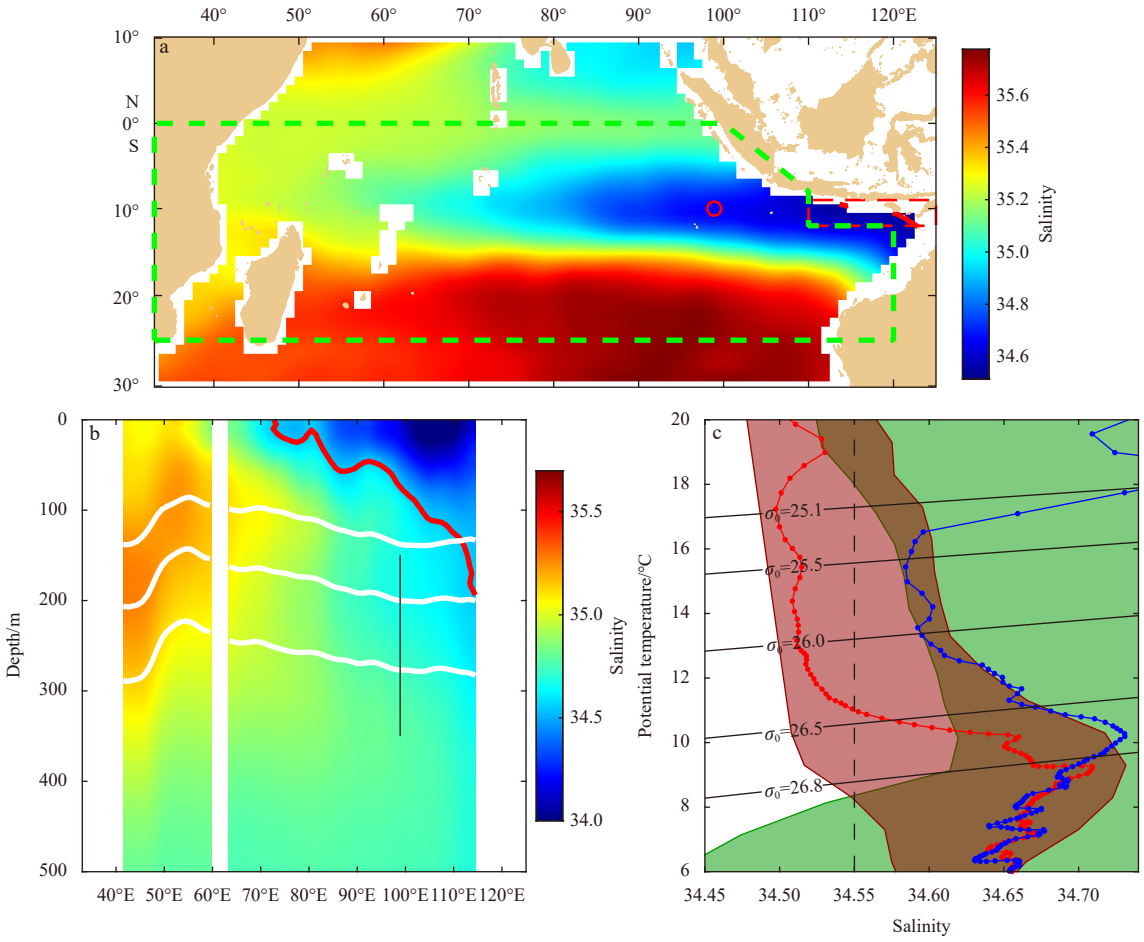

Fig. 5. The background salinity and potential temperature and salinity (*T*-*S*) diagrams of observation and background. a. Annual mean salinity distribution of the BOA_ARGO on the 26.0 σ_0 surface in the south Indian Ocean. The red circle represents the location of the cruise-observed subthermocline eddy (STE). b. Depth-longitude plot of annual mean salinity of the BOA_ARGO along 10°S. The black bar represents the location of the cruise-observed STE. The white contours from top to bottom represent the isopycnals of 25.0 σ_0, 26.0 σ_0, and 26.5 σ_0, respectively. The red contour in a and b represent isohaline of 34.55 (isohaline of 34.55 was discontinuous in a because of the annual mean Argo data that was unavailable near the coast). c. *T*-*S* diagrams of water mass within the areas of red and green dashed boxes in a are shown as red and green shadings, respectively. The red dotted line shows the *T*-*S* distribution in the cruise-observed STE center (station s-1), and the blue dotted line represents the results measured out of the STE (station s-4). The contours show the potential density. The vertical dashed line indicates the isohaline of 34.55.

STE using only the lens structure outlined by the isopycnals derived from Argo profiles. Li et al. (2017b) detected cold and fresh STEs in the northwestern Pacific mainly by examining the STE-induced characteristic salinity anomaly of Argo profiles. Because the cruise-observed STE was characterized as the low-salinity ITF core water, we first tried to find the low-salinity signal in the SETIO using the Argo float data. We individually checked the quality of the Argo profiles. Only those flagged as good (Argo quality flag 1) were retained for the analysis. The salinity profiles were interpolated onto a set of density surfaces between 25.1 σ_0 (~130 m) and 26.8 σ_0 (~400 m) surfaces with an interval of 0.01 kg/m^3. As the salinity of cruise-observed STE reached a minimum at around 26.0 σ_0, we selected the profiles with salinity below 34.55 at 26 σ_0 and termed them as low-salinity profiles (LSPs). From a total of 20 993 profiles (in the area covering 4°–16°S, 80°–123°E), we identified a total of 993 (4.7%) LSPs. The spatial distribution of these LSPs is shown in Fig. 6a. The distribution of LSPs extended northwestward from the eastern coastal waters to west of 80°E and north of 4°S.

We then calculated, for each Argo float measuring successive profiles, the potential density as a function of the depth and the time. We identified the STEs carrying ITF water by finding low-salinity cores (<34.55) inside a lens, that is, the isopycnals above the "low-salinity core" were domed upward, whereas those below this core were depressed (as detailed in Zhang et al. (2017)). Only one STE was well captured by five successive profiles of the same Argo float (WMO ID 5900860). As shown in Fig. 7, the captured Argo-observed STE was located off the northwest edge of a surface eddy.

The temperature and salinity distributions of the Argo-observed STE are shown in Fig. 8. The STE was located basically between 100 m and 300 m. The temperature and salinity anomalies against σ_0 showed a Gaussian-like distribution and had a peak value at the 26.0 σ_0 surface, which was similar to that of the cruise-observed STE. The *T*-*S* distributions of the cruise- and Argo-observed STEs were close between 25.5 σ_0 and 26.5 σ_0 surfaces (Fig. 6b).

4 Discussion

The generation mechanism of STEs has been broadly discussed (D'Asaro, 1988; Spall, 1995; Spall and Price, 1998; Zhurbas et al., 2004; Kurian et al., 2011; Pelland et al., 2013). The two most famous STE generation mechanisms are the front-induced water parcel subduction and topography-induced current instability. As shown in Fig. 5, the area occupied by the low-salinity ITF water decreased with depth. The isohaline of 34.55 extended westward to the west of 80°E at the sea surface, whereas it was limited to the coastal areas at the isopycnal surfaces where we had observed the STEs. Therefore, even though the observed STEs were characterized by low-salinity water, which should have come only from the ITF water in the SETIO, the observed STEs may have had different origins and generation mechanisms. The STEs may originate from the coastal area near the Ombai Strait, the Lombok Strait, and the Timor Passage because of the interaction of the current and abrupt topography (termed as coastal origin). Previous theoretical modeling studies have suggested that the coastal area around the Timor passage was favorable for STE

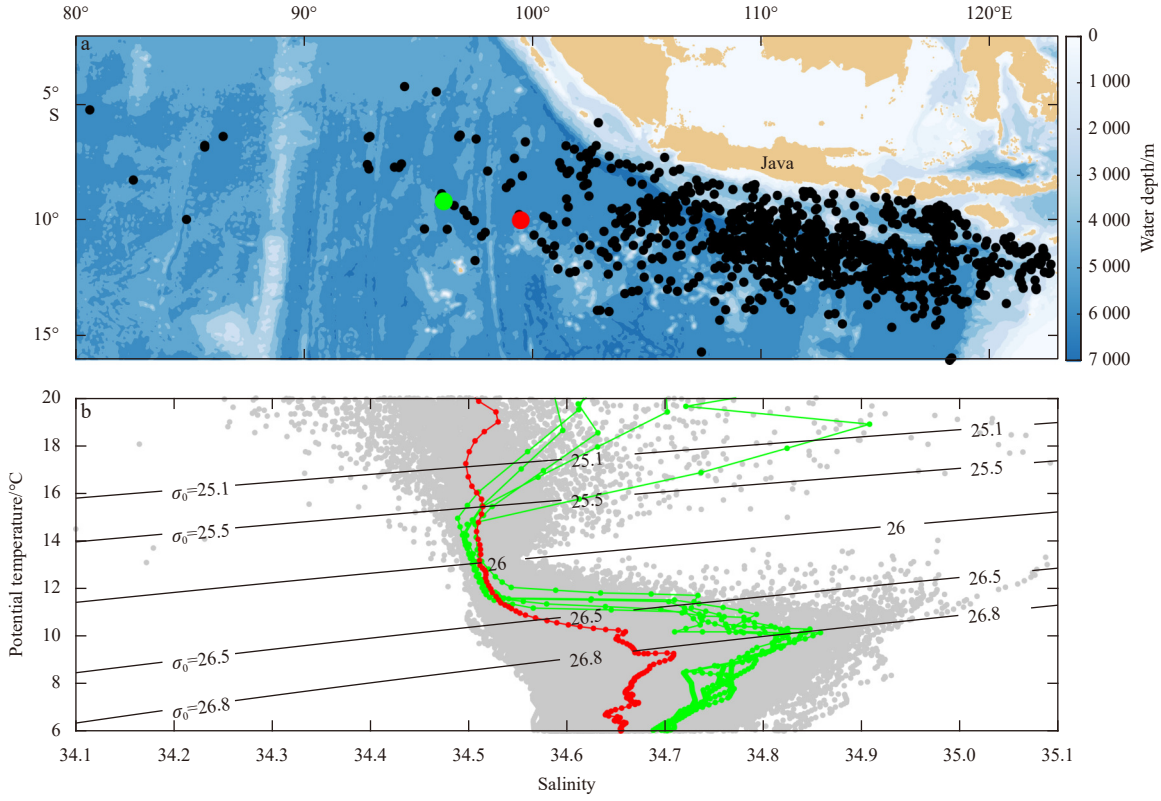

Fig. 6. Spatial distribution and potential temperature and salinity (*T*-*S*) diagrams of the identified low-salinity Argo profiles. a. Spatial distribution of the identified low-salinity Argo profiles (black dots). The red and green dots show the location of the cruise- and Argo-observed subthermocline eddy (STE), respectively. The color codes show the topography. b. *T*-*S* plot. The gray dots represent the *T*-*S* distribution of the identified low-salinity Argo profiles corresponding to the black dots in a. Red and green dotted lines show the observed *T*-*S* distributions within the cruise-observed (at station s-1) and Argo-observed (on March 26, 2006) STE, respectively.

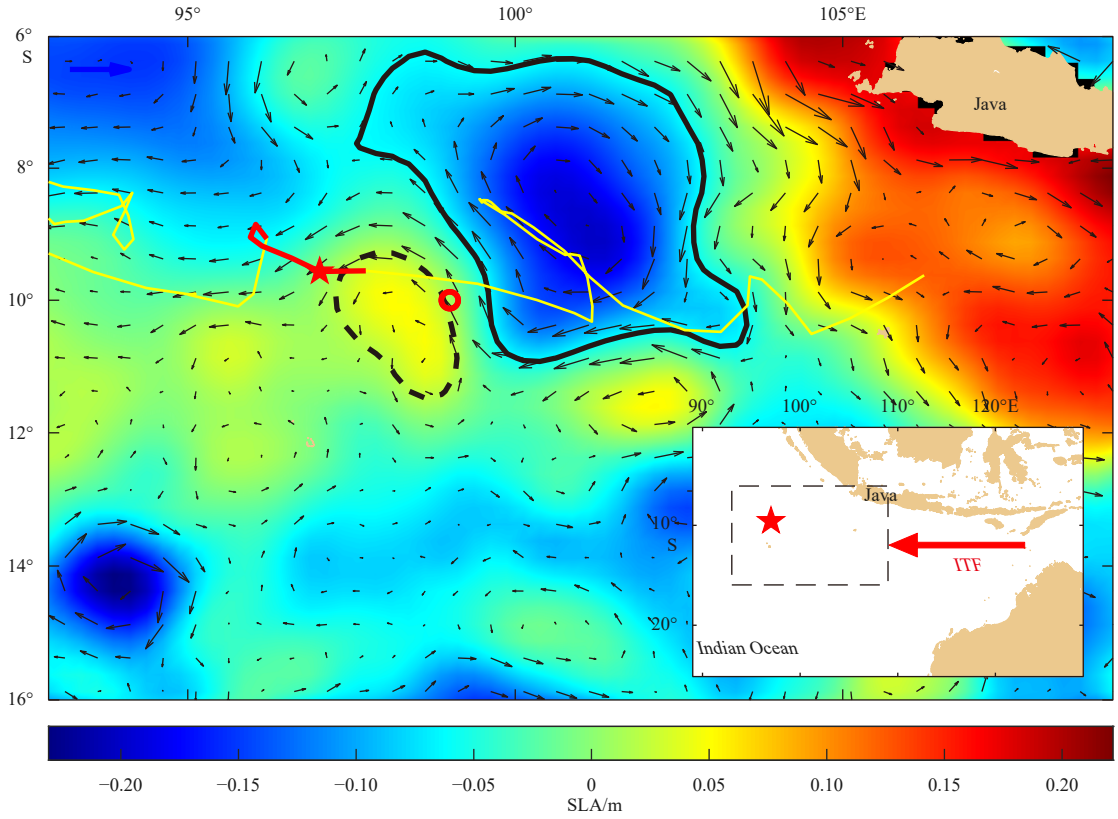

Fig. 7. The Argo float trajectory and the sea-level anomaly (SLA). The yellow line indicates the trajectory of the Argo float with platform number 5900860. The red part indicates the position where the Argo-observed subthermocline eddy (STE) was detected. Color codes show SLA on March 26, 2006, when the Argo float was at the location indicated by the red star (also in the inset). Black arrows represent geostrophic current vectors. Black solid and dashed contours show the outermost enclosed SLA isolines of the surface anticyclonic eddy and cyclonic eddy, respectively. The red circle indicates the cruise-observed STE. The observation area is shown in an inset on the bottom right corner. ITF: Indonesian Throughflow.

generation (Nof et al., 2002). In addition, the observed STEs also may originate from the sea surface in open ocean as well because of the front-induced subduction (termed as local origin because the two observed STEs are all observed in the open ocean). As suggested by Sarkar et al. (2016), the surface-layer low-salinity water from river input and precipitation in the northern Bay of Bengal would generate a salinity front. The frontogenesis in the mixed layer produced low PV core, which then would be subducted by the ageostrophic circulation and advected beneath the main thermocline. The STEs finally formed through balanced adjustment. In addition, the surface eddies were abundant in the SETIO (Yang et al., 2015) and submesoscale instabilities generated in the mixed layer front of the surface eddies could lead to the subduction of low PV fluid (Brannigan et al., 2017). Thus, we speculated that the front generated by the surface eddies also played a role in the STE formation.

To discover more clues on the origin and generation of the STEs, we revisited the distribution of LSPs. Because the ITF water gradually diffused and mixed with surrounding high-salinity water as it was advected westward, the LSPs, except for those detected near the eastern coastal waters, should have revealed the existence of a low-salinity ITF water parcel. The surface and subsurface eddies could generate closed PV contours on an isopycnal surface and the water parcels trapped inside the closed PV contour would be protected from mixing with the surrounding water (Zhang et al., 2014). Therefore, the LSPs detected away from the eastern coastal waters should be inside either a surface eddy or a subsurface eddy.

In this study, we believed that an LSP would be located within and carried by a surface eddy when the distance between the LSP and the nearest eddy center was smaller than the eddy radius L_s, which is defined as the radius of a circle whose area is equal to that enclosed by the contour of maximum axial speed (Chelton et al., 2011). Figure 9 shows some examples of the relative location of LSPs and surface eddies or subsurface eddies. The locations and radiuses of surface eddies were from META data. We then classified the LSPs into three types: inside a surface CE (Fig. 9c), inside a surface AE (Fig. 9d), and outside a surface eddy (Figs 9a, b). The LSPs located outside a surface eddy could be associated with the STE.

Figure 9e shows the spatial distribution of the LSPs located inside and outside surface eddies. The LSPs were distributed in the area covering 4°–16°S, and 80°–120°E. The distribution of both LSPs located inside and outside surface eddies extended from southeast to northwest and was consistent with the distribution of the EKE.

Figure 10 shows the zonal distribution of three types of LSPs. Because eddies in the SETIO propagated westward, we examined the zonal distribution of LSPs from east to west. In the area east of 117°E, most of the LSPs were outside the surface eddies because the ITF just flowed into the Indian Ocean and the EKE was weak. From 115°E to 113°E, the ratio of the LSPs outside the surface eddies to that inside the surface eddies exhibited an inverse relationship with the EKE (Fig. 10b). More LSPs were loc-

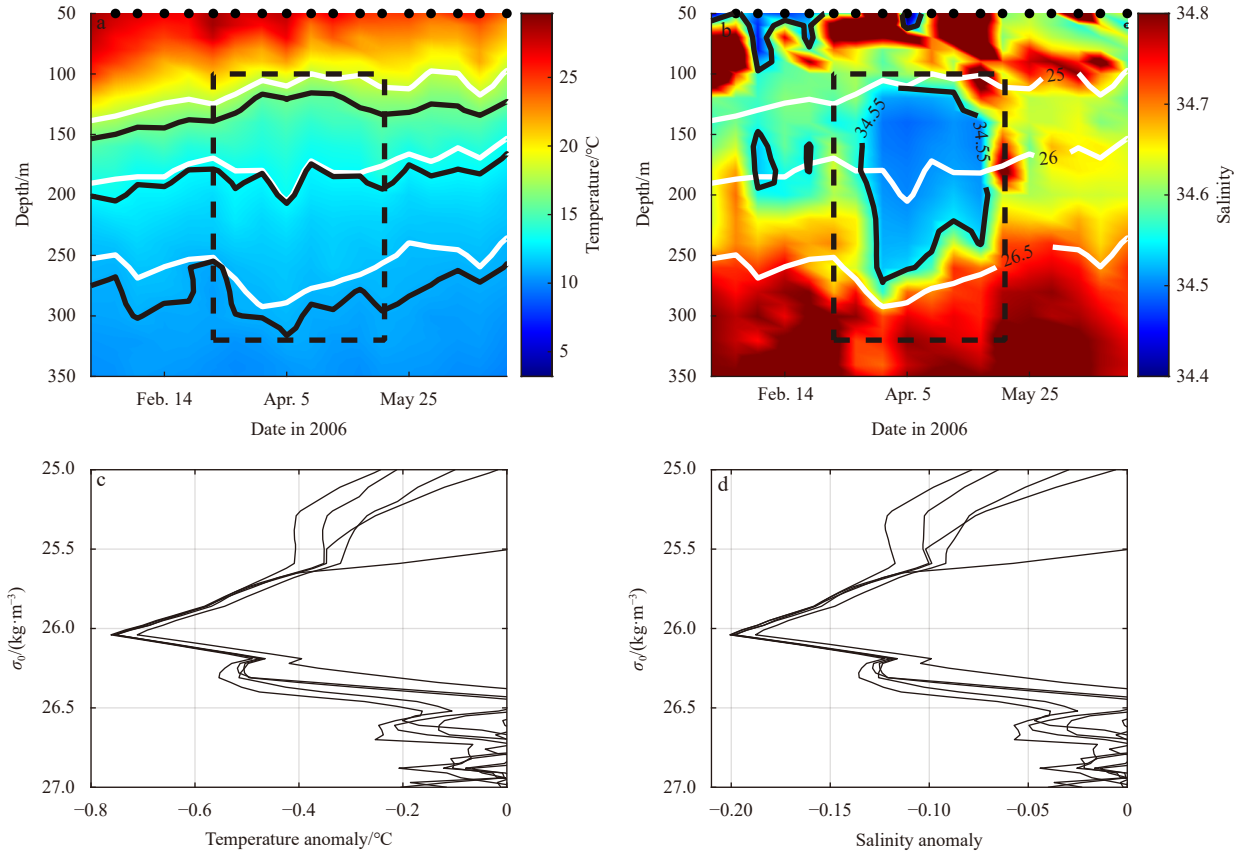

Fig. 8. Depth-time plots of temperature (a) and salinity (b) of the Argo-observed STE. Black contours denote isotherms of 16℃, 13℃, and 11℃ in a, and isohalines of 34.55 in b, respectively. White contours denote isopycnals of 25 σ_0, 26 σ_0, and 26.50 σ_0. c and d are the temperature and salinity anomalies generated by the Argo-observed STE (the temperature and salinity observed in the STE, minus those observed out of the STE).

ated inside the surface eddies when the EKE became stronger. About two-thirds of the LSPs, however, were still located outside surface eddies. Even if an LSP was defined as being inside a surface eddy when the distance between the LSP and the nearest eddy center was smaller than $2L_s$, at least one-third of the LSPs were outside the surface eddy. This result suggested that a lot of STEs could be generated in coastal waters.

From 113°E to the west, the EKE began to decrease whereas the ratio of the LSPs outside the surface eddies to that inside surface eddies increased (Fig. 10b). This suggested that the STE may have a longer lifespan or that new STEs were generated in the open ocean (local origin). We therefore tried to find clues regarding to the possibility and mechanism of the local origin of the STE.

The CTD observations near the sea surface are shown in Fig. 11. The water in the upper 50 m was mixed well in the STE area (stations s-1 and s-2), whereas only the water in the upper 30 m was mixed well outside the STE area (stations s-3, s-4, and s-5).

The mixed layer depth is controlled by many air-sea dynamic processes. The diurnal restratification (Brainerd and Gregg, 1993), sea surface wind (Nagai et al., 2012; Yang et al., 2019c), and waves (Qiao et al., 2004, 2016; Babanin, 2006; Huang and Qiao, 2010; Huang et al., 2012) are the most well-known processes affecting the mixed layer depth. Because the CTD observation at stations s-2, s-3, and s-4 were conducted during the daytime, whereas those at stations s-1 and s-5 were conducted during the nighttime, the difference in mixed layer depth at those five stations should not be associated with diurnal restratification. The sea surface wind speed (~5 m/s) and the significant wave height (~1.9 m) during the observation at the five stations were small and had no significant change. The enhanced near-surface mixing in s-1 and s-2 also should not be associated with sea surface winds or waves.

A more plausible explanation would seem to be that the mixed layer depth was associated mainly with the surface eddies, because the observation transect extended from the surface CE toward the adjacent surface AE, and the surface AE (CE) can deepen (shallow) the mixed layer depth (Yang et al., 2017). The mixed layer depth may be even deeper at the surface AE. A deeper mixed layer, along with the front generated by surface eddies, is favored for the submesoscale instabilities and subduction of surface water parcels (Brannigan et al., 2017). In addition, because the outcropping isopycnals of surface AEs extended deeper into the thermocline, modeling result suggest that the subduction of low PV fluid in the surface AEs is much stronger than that in surface CEs (Brannigan et al., 2017). This theory has been used to explain the finding of STEs in surface AEs (Baird and Ridgway, 2012; Brannigan et al., 2017). In this study, the outermost enclosed SLA isolines were used to show the edge of the surface eddies (Figs 2 and 7), and both of the observed STEs were located near a surface AE. However, the symmetric and rotating background current field (Fig. 3) suggested that the cruise-observed STE may have been located within the surface AE. As outlined by the 34.55 isoline shown in Fig. 4b, the core of cruise-observed

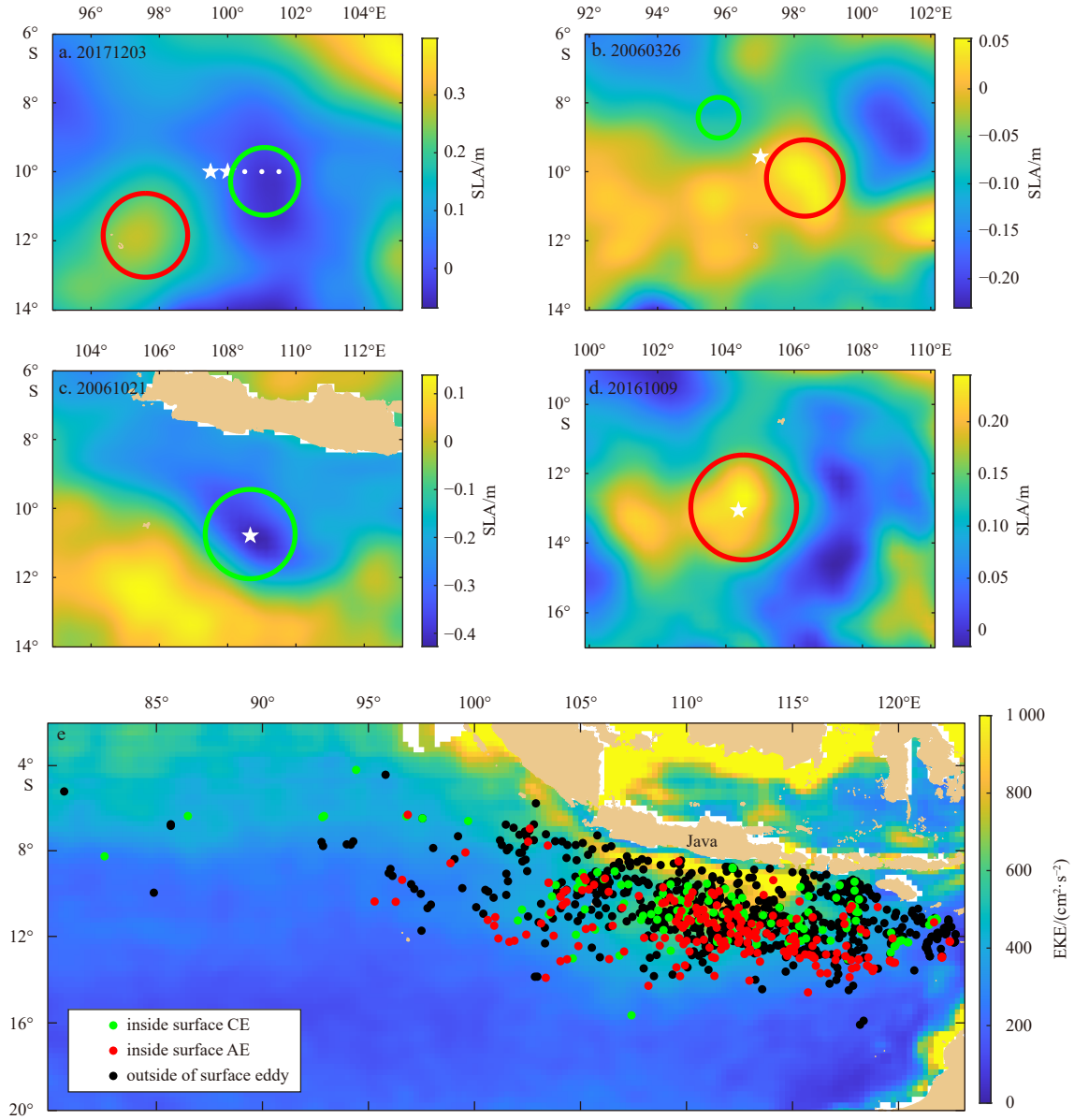

Fig. 9. The relative locations between low-salinity profiles (LSPs) and surface eddies and the distribution of different LSPs. a–d. Examples showing the relative locations between LSPs and surface eddies. The white stars indicate the positions of LSPs. The green and red circles indicate the adjacent surface cyclonic eddy (CE) and anticyclonic eddy (AE), respectively. Color codes show sea-level anomaly (SLA) on the day indicated in the upper left corner. a. The two stars indicate the stations s-1 and s-2, which are located inside the cruise-observed subthermocline eddy (STE) and outside of the adjacent surface CE. The white points indicate stations s-3, s-4, and s-5 from left to right. b. The star indicates the LSP located inside the Argo-observed STE and outside of adjacent surface eddies. c. An LSP, captured by Argo float with platform number 5900462, is located inside a surface CE. d. An LSP, captured by Argo float with platform number 5905018, is located inside a surface AE. e. The distribution of LSPs located inside surface CEs, AEs, and outside the surface eddies. The color codes show the eddy kinetic energy (EKE).

STE was ventilated with surface low-salinity water. These clues may suggest that the STEs can be generated in the open ocean because of surface water subduction generated in the mixed layer front of surface AEs and may be located within a surface AE.

Because the possible generation of STE in surface AEs suggested that the subsurface ITF water transport may be associated with both surface eddies and STEs, it was difficult to evaluate the respective contributions of surface eddies and the STEs to ITF water transport with the limited observations in this study. Further studies with intensive observation (such as rapid-sampling Argo floats and mooring) and fine resolution modeling (submesocale permitting) are needed to better evaluate the role of the STEs.

5 Summary

In this study, we observed an STE carrying fresh ITF water with concurrent CTD and VADCP measurements obtained during a cruise conducted in the SETIO in December 2017. The speed radius, mean Rossby number, and Burger number of the cruise-observed STE were 55 km, –0.7, and 2.4, respectively, which indicated that the STE was a submesoscale eddy. By examining Argo float data, we further identified another STE that

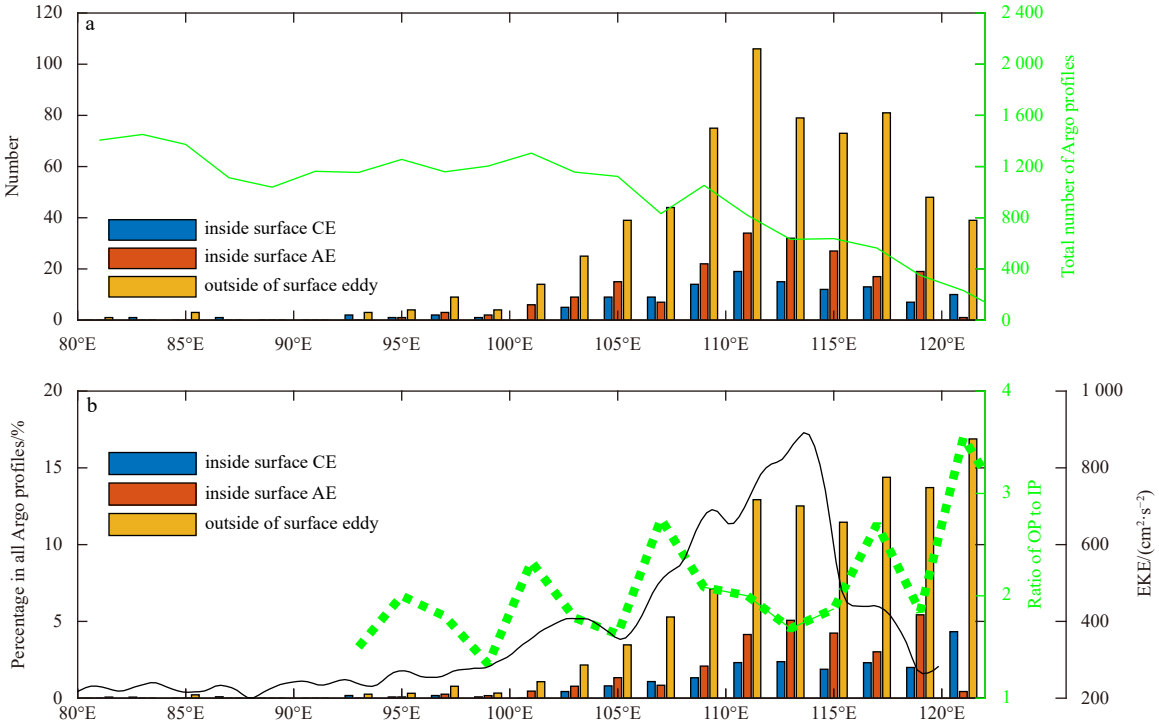

Fig. 10. The zonal distribution of low-salinity profiles (LSPs). a. The blue, red, and yellow bars show the zonal distribution of the number of LSPs located inside cyclonic eddys (CEs), anticyclonic eddys (AEs), and outside of surface eddies, respectively. The green line indicates the zonal distribution of the number of the total Argo profiles. The zonal bin is 2°. b. The blue, red, and yellow bars show the percentage of LSPs located inside CEs, AEs, and outside of surface eddies in the total Argo profiles. The green line indicates the ratio of the LSPs located outside surface eddies (OP) to that located inside surface eddies (IP). The green line becomes a dotted line when the Argo float number is relatively small. The black line indicates the eddy kinetic energy (EKE) along 10°S.

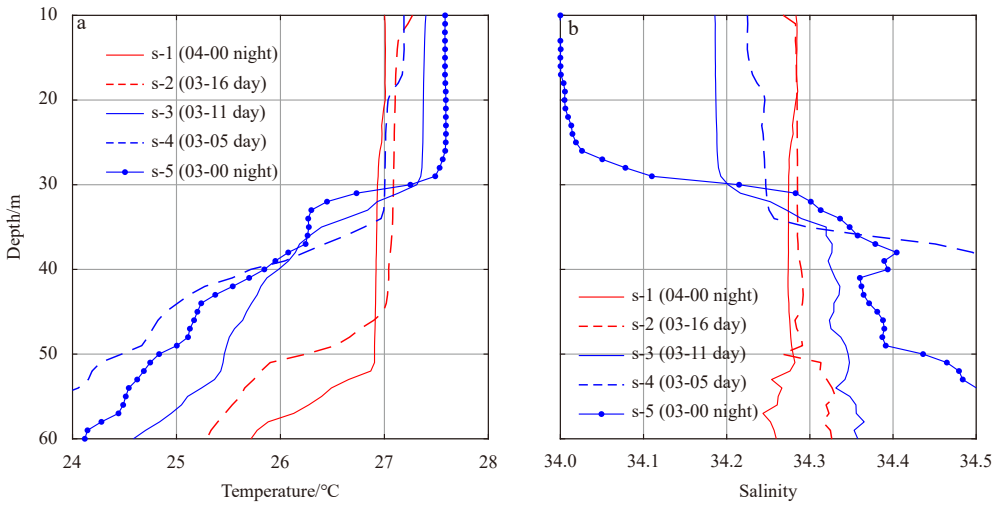

Fig. 11. Temperature (a) and salinity (b) profiles observed at the five stations. The local observation time (DD-HH) is denoted.

carried ITF water and was well captured by five successive profiles of the same Argo float. Both of the STEs had a vertical scale of about 200 m and were characterized by a low-salinity core (<34.55) within a lens feature.

The LSPs were defined as the Argo profiles detecting low-salinity ITF water at the 26.0σ_0 isopycnal surface. Because the low-salinity ITF water parcels should be carried only by surface eddies and the STEs in the area away from eastern coastal waters, the distribution of LSPs could be used to analyze the distribution, origin, and generation mechanism of the STEs carrying ITF water. The results suggested that the STEs may be widely distributed in the SETIO and may play a role in ITF water transport. Furthermore, topography-current interaction at the eastern coastal waters and front-induced subduction in the area away from coastal waters were possible STE generation mechanisms.

This study shed light on the structure, generation mechanism, and distribution of the STEs carrying ITF water. Because of limited data, however, further *in situ* observation and modeling studies are needed to present better knowledge of the detailed dynamics of STEs.

Acknowledgements

We thank all onboard crews of R/V *Xiangyanghong 18* and the two anonymous reviewers. The cruise data can be obtained at this website (https://jmp.sh/wWLYFUk). The sources of other data are provided in Section 2.

References

Babanin A V. 2006. On a wave-induced turbulence and a wave-mixed upper ocean layer. Geophysical Research Letters, 33(20): L20605, doi: 10.1029/2006GL027308

Baird M E, Ridgway K R. 2012. The southward transport of sub-mesoscale lenses of Bass Strait Water in the centre of anti-cyclonic mesoscale eddies. Geophysical Research Letters, 39(2), doi: 10.1029/2011GL050643

Bashmachnikov I, Neves F, Calheiros T, et al. 2015. Properties and pathways of Mediterranean water eddies in the Atlantic. Progress in Oceanography, 137: 149–172, doi: 10.1016/j.pocean.2015.06.001

Brainerd K E, Gregg M C. 1993. Diurnal restratification and turbulence in the oceanic surface mixed layer: 1. Observations. Journal of Geophysical Research, 98(C12): 22645–22656, doi: 10.1029/93JC02297

Brannigan L, Marshall D P, Garabato A C N, et al. 2017. Submesoscale instabilities in mesoscale eddies. Journal of Physical Oceanography, 47(12): 3061–3085, doi: 10.1175/JPO-D-16-0178.1

Chelton D B, DeSzoeke R A, Schlax M G, et al. 1998. Geographical variability of the first baroclinic Rossby radius of deformation. Journal of Physical Oceanography, 28(3): 433–460, doi: 10.1175/1520-0485(1998)028<0433:GVOTFB>2.0.CO;2

Chelton D B, Schlax M G, Samelson R M. 2011. Global observations of nonlinear mesoscale eddies. Progress in Oceanography, 91(2): 167–216, doi: 10.1016/j.pocean.2011.01.002

Contreras M, Pizarro O, Dewitte B, et al. 2019. Subsurface mesoscale eddy generation in the ocean off central chile. Journal of Geophysical Research: Oceans, 124(8): 5700–5722, doi: 10.1029/2018JC014723

D'Asaro E A. 1988. Generation of submesoscale vortices: A new mechanism. Journal of Geophysical Research: Oceans, 93(C6): 6685–6693, doi: 10.1029/JC093iC06p06685

Feng Ming, Wijffels S. 2002. Intraseasonal variability in the south equatorial current of the East Indian Ocean. Journal of Physical Oceanography, 32(1): 265–277, doi: 10.1175/1520-0485(2002)032<0265:IVITSE>2.0.CO;2

Godfrey J S. 1996. The effect of the Indonesian Throughflow on ocean circulation and heat exchange with the atmosphere: A review. Journal of Geophysical Research: Oceans, 101(C5): 12217–12237, doi: 10.1029/95JC03860

Gordon A L, Susanto R D, Vranes K. 2003. Cool Indonesian Throughflow as a consequence of restricted surface layer flow. Nature, 425(6960): 824–828, doi: 10.1038/nature02038

Hu Zhentao, Ma Xiao, Peng Yingyu, et al. 2022. A large subsurface anticyclonic eddy in the eastern equatorial Indian Ocean. Journal of Geophysical Research: Oceans, 127(3): e2021JC018130, doi: 10.1029/2021JC018130

Huang Xiaolong, Jing Zhiyou, Zheng Ruixi, et al. 2020. Dynamical analysis of submesoscale fronts associated with wind-forced offshore jet in the western South China Sea. Acta Oceanologica Sinica, 39(11): 1–12, doi: 10.1007/s13131-020-1671-4

Huang Chuanjiang, Qiao Fangli. 2010. Wave-turbulence interaction and its induced mixing in the upper ocean. Journal of Geophysical Research: Oceans, 115(C4): C04026, doi: 10.1029/2009JC005853

Huang Chuanjiang, Qiao Fangli, Dai Dejun, et al. 2012. Field measurement of upper ocean turbulence dissipation associated with wave-turbulence interaction in the South China Sea. Journal of Geophysical Research: Oceans, 117(C11): C00J09, doi: 10.1029/2011JC007806

Kurian J, Colas F, Capet X, et al. 2011. Eddy properties in the California Current System. Journal of Geophysical Research: Oceans, 116(C8): C08027, doi: 10.1029/2010JC006895

Li Hong, Xu Fanghua, Zhou Wei, et al. 2017a. Development of a global gridded Argo data set with Barnes successive corrections. Journal of Geophysical Research: Oceans, 122(2): 866–889, doi: 10.1002/2016JC012285

Li Cheng, Zhang Zhiwei, Zhao Wei, et al. 2017b. A statistical study on the subthermocline submesoscale eddies in the northwestern Pacific Ocean based on Argo data. Journal of Geophysical Research: Oceans, 122(5): 3586–3598, doi: 10.1002/2016JC012561

Makarim S, Sprintall J, Liu Zhiyu, et al. 2019. Previously unidentified Indonesian Throughflow pathways and freshening in the Indian Ocean during recent decades. Scientific Reports, 9(1): 7364, doi: 10.1038/s41598-019-43841-z

Mcwilliams J C. 2016. Submesoscale currents in the ocean. Proceedings of the Royal Society A: Mathematical, Physical and Engineering Sciences, 472(2189): 20160117, doi: 10.1098/rspa.2016.0117

Nagai T, Tandon A, Yamazaki H, et al. 2012. Direct observations of microscale turbulence and thermohaline structure in the Kuroshio Front. Journal of Geophysical Research: Oceans, 117(C8): C08013, doi: 10.1029/2011JC007228

Nof D, Pichevin T, Sprintall J. 2002. "Teddies" and the origin of the leeuwin current. Journal of Physical Oceanography, 32(9): 2571–2588, doi: 10.1175/1520-0485(2002)032<2571:TATOOT>2.0.CO;2

Pelland N A, Eriksen C C, Lee C M. 2013. Subthermocline eddies over the Washington continental slope as observed by seagliders, 2003–09. Journal of Physical Oceanography, 43(10): 2025–2053, doi: 10.1175/JPO-D-12-086.1

Qiao Fangli, Yuan Yeli, Deng Jia, et al. 2016. Wave–turbulence interaction-induced vertical mixing and its effects in ocean and climate models. Philosophical Transactions of the Royal Society A: Mathematical, Physical and Engineering Sciences, 374(2065): 20150201, doi: 10.1098/rsta.2015.0201

Qiao Fangli, Yuan Yeli, Yang Yongzeng, et al. 2004. Wave-induced mixing in the upper ocean: Distribution and application to a global ocean circulation model. Geophysical Research Letters, 31(11): L11303, doi: 10.1029/2004GL019824

Sarkar S, Pham H T, Ramachandran S, et al. 2016. The interplay between submesoscale instabilities and turbulence in the surface layer of the bay of Bengal. Oceanography, 29(2): 146–157, doi: 10.5670/oceanog.2016.47

Shapiro G I, Meschanov S L. 1991. Distribution and spreading of Red Sea Water and salt lens formation in the northwest Indian Ocean. Deep Sea Research Part A. Oceanographic Research Papers, 38(1): 21–34, doi: 10.1016/0198-0149(91)90052-H

Song Qian, Gordon A L, Visbeck M. 2004. Spreading of the Indonesian Throughflow in the Indian Ocean. Journal of Physical Oceanography, 34(4): 772–792, doi: 10.1175/1520-0485(2004)034<0772:SOTITI>2.0.CO;2

Song Bo, Wang Huizan, Chen Changlin, et al. 2019. Observed subsurface eddies near the Vietnam coast of the South China Sea. Acta Oceanologica Sinica, 38(4): 39–46, doi: 10.1007/s13131-019-1412-8

Spall M A. 1995. Frontogenesis, subduction, and cross-front exchange at upper ocean fronts. Journal of Geophysical Research, 100(C2): 2543–2557, doi: 10.1029/94JC02860

Spall M A, Price J F. 1998. Mesoscale variability in Denmark Strait: The PV outflow hypothesis. Journal of Physical Oceanography, 28(8): 1598–1623, doi: 10.1175/1520-0485(1998)028<1598:mvidst>2.0.co;2

Sprintall J, Wijffels S E, Molcard R, et al. 2009. Direct estimates of the Indonesian Throughflow entering the Indian Ocean: 2004–2006. Journal of Geophysical Research: Oceans, 114(C7): C07001, doi: 10.1029/2008JC005257

Valsala V K, Ikeda M. 2007. Pathways and effects of the Indonesian Throughflow water in the Indian Ocean using particle trajectory and tracers in an OGCM. Journal of Climate, 20(13): 2994–3017, doi: 10.1175/JCLI4167.1

Van Sebille E, Sprintall J, Schwarzkopf F U, et al. 2014. Pacific-to-Indian Ocean connectivity: Tasman leakage, Indonesian Through-

flow, and the role of ENSO. Journal of Geophysical Research: Oceans, 119(2): 1365–1382, doi: 10.1002/2013JC009525

Wang Lu, Zhou Lei, Xie Lingling, et al. 2019. Seasonal and interannual variability of water mass sources of Indonesian Throughflow in the Maluku Sea and the Halmahera Sea. Acta Oceanologica Sinica, 38(4): 58–71, doi: 10.1007/s13131-019-1413-7

Yang Guang, Yu Weidong, Yuan Yeli, et al. 2015. Characteristics, vertical structures, and heat/salt transports of mesoscale eddies in the southeastern tropical Indian Ocean. Journal of Geophysical Research: Oceans, 120(10): 6733–6750, doi: 10.1002/2015JC011130

Yang Guang, Zhao Xia, Li Yuanlong, et al. 2019a. Chlorophyll variability induced by mesoscale eddies in the southeastern tropical Indian Ocean. Journal of Marine Systems, 199: 103209, doi: 10.1016/j.jmarsys.2019.103209

Yang Qingxuan, Zhao Wei, Liang Xinfeng, et al. 2017. Elevated mixing in the periphery of mesoscale eddies in the South China Sea. Journal of Physical Oceanography, 47(4): 895–907, doi: 10.1175/JPO-D-16-0256.1

Yang Guangbing, Zheng Quanan, Xiong Xuejun, et al. 2019b. Subsurface cyclonic eddies observed in the southeastern tropical Indian Ocean. Journal of Geophysical Research: Oceans, 124(10): 7247–7260, doi: 10.1029/2019JC015381

Yang Guangbing, Zheng Quanan, Yuan Yeli, et al. 2019c. Effect of a mesoscale eddy on surface turbulence at the Kuroshio Front in the East China Sea. Journal of Geophysical Research: Oceans, 124(3): 1763–1777, doi: 10.1029/2018JC014672

Zhang Zhiwei, Li Peiliang, Xu Lixiao, et al. 2015. Subthermocline eddies observed by rapid-sampling Argo floats in the subtropical northwestern Pacific Ocean in Spring 2014. Geophysical Research Letters, 42(15): 6438–6445, doi: 10.1002/2015GL064601

Zhang Zhiwei, Liu Zhiyu, Richards K, et al. 2019. Elevated diapycnal mixing by a subthermocline eddy in the western equatorial Pacific. Geophysical Research Letters, 46(5): 2628–2636, doi: 10.1029/2018GL081512

Zhang Zhengguang, Wang Wei, Qiu Bo. 2014. Oceanic mass transport by mesoscale eddies. Science, 345(6194): 322–324, doi: 10.1126/science.1252418

Zhang Xincheng, Zhang Zhiwei, McWilliams J C, et al. 2022. Submesoscale coherent vortices observed in the northeastern South China Sea. Journal of Geophysical Research: Oceans, 127(2): e2021JC018117, doi: 10.1029/2021JC018117

Zhang Zhengguang, Zhang Yu, Wang Wei. 2017. Three-compartment structure of subsurface-intensified mesoscale eddies in the ocean. Journal of Geophysical Research: Oceans, 122(3): 1653–1664, doi: 10.1002/2016JC012376

Zheng Quanan, Lin Hui, Meng Junmin, et al. 2008. Sub-mesoscale ocean vortex trains in the Luzon Strait. Journal of Geophysical Research: Oceans, 113(C4): C04032, doi: 10.1029/2007JC004362

Zheng Quanan, Xie Lingling, Xiong Xuejun, et al. 2020. Progress in research of submesoscale processes in the South China Sea. Acta Oceanologica Sinica, 39(1): 1–13, doi: 10.1007/s13131-019-1521-4

Zhou Lei, Murtugudde R, Jochum M. 2008. Seasonal influence of Indonesian Throughflow in the southwestern Indian Ocean. Journal of Physical Oceanography, 38(7): 1529–1541, doi: 10.1175/2007JPO3851.1

Zhurbas V, Stipa T, Mälkki P, et al. 2004. Generation of subsurface cyclonic eddies in the southeast Baltic Sea: Observations and numerical experiments. Journal of Geophysical Research: Oceans, 109(C5): C05033, doi: 10.1029/2003JC002074